

A Fermi arc quantum ladder

Tyler A. Cochran ^{*},¹ Guoqing Chang ^{*},¹ Ilya Belopolski ^{*},¹ Kaustuv Manna,² Daniel S. Sanchez,¹ Zijia Chéng,¹ Jia-Xin Yin,¹ Horst Borrmann,² Jonathan Denlinger,³ Claudia Felser,² Hsin Lin,⁴ and M. Zahid Hasan [†]^{1,5,6}

¹*Laboratory for Topological Quantum Matter and Spectroscopy (B7),
Department of Physics, Princeton University, Princeton, New Jersey 08544, USA*

²*Max Planck Institute for Chemical Physics of Solids, Dresden, Germany*

³*Advanced Light Source, Lawrence Berkeley National Laboratory, Berkeley, CA 94720, USA*

⁴*Institute of Physics, Academia Sinica, Taipei 11529, Taiwan*

⁵*Princeton Institute for Science and Technology of Materials,
Princeton University, Princeton, New Jersey 08544, USA*

⁶*Lawrence Berkeley National Laboratory, Berkeley, CA 94720, USA*

^{*}These authors contributed equally to this work

[†] Corresponding Author: mzhasan@princeton.edu

Known topological quantum matter, including topological insulators and Dirac/Weyl semimetals, often hosts robust boundary states in the gaps between bulk bands in energy-momentum space. Beyond one-gap systems, quantum crystals may also feature more than one inter-band gap. The manifestation of higher-fold topology with multiple nontrivial gaps in quantum materials remains elusive. In this work, we leverage a photoemission spectroscopy probe to discover the multi-gap topology of a chiral fermion material. We identify two sets of chiral surface states. These Fermi arcs exhibit an emergent ladder structure in energy-momentum space, unprecedented in topological materials. Furthermore, we determine the multi-gap chiral charge $C = (2, 2)$. Our results provide a general framework to explore future complex topological materials.

Topological phases have taken center stage in condensed matter physics and material science, due to their exotic quantum properties [1–10]. In crystals, nontrivial topology is manifest in the bulk-boundary correspondence of their electronic structure, which specifies that topologically nontrivial bulk bands give rise to protected surface states. These surface states, in turn, encode the topology of the bulk bands [2, 3, 7]. The understanding of this correspondence over the past decades has led to the discovery of many types of topological quantum matter, including topological insulators with Dirac surface states [2–4], magnetic topological insulators with chiral edge modes [5, 6], and Weyl semimetals with helicoid surface Fermi arcs [7–10]. Each of these discoveries has opened a subfield with immense research activity. These examples are all composed of a single set of surface states in the inter-band gap between two bulk bands; see Fig. 1(a),(b). Here we use the term gap to indicate an energy separation between two bands, which is topologically equivalent to a global band gap, i.e. it can be continuously deformed into a global gap without any bands crossing. A theoretical frontier in the field is the properties of topological phases in multi-gap systems, which are theoretically predicted to exhibit novel quantum properties such as exotic Landau level structure and unusual optical/transport properties [11–18]. By leveraging the bulk-boundary correspondence, surface sensitive experimental techniques are critical to determine the unique topology of multi-gap topological crystals. Despite intensive investigations, no previous experimental observation has determined the set of topological invariants of multiple nontrivial band gaps, which precisely identify the global ground state. In this study, we use ultra-violet angle-resolved photoemission spectroscopy (ARPES) to study the chiral substitutional alloy A_xB_ySi where A and B are group 9 and 10 elements, respectively. We directly and clearly observe a Fermi arc ladder of surface states.

To attain an experimental realization of the Fermi arc ladder, we consider semimetals that host higher-fold chiral fermions, which can be understood as a generalization of more familiar Weyl fermions. For Weyl fermions, one topological invariant, the chiral charge C , is defined within the band gap on k -space manifolds enclosing a the two-fold degeneracy; see Fig. 1(a). As a consequence, one set of boundary states is topologically protected within the gap; see Fig. 1(b). By extending this paradigm to higher-fold fermions, the set of possibilities becomes more diverse. Dirac-like nonchiral fermions have a chiral charge of zero in each gap [12, 19–22], whereas Weyl-like chiral fermions have nonzero chiral charge in multiple gaps [11, 13–16]. For an N -fold chiral fermion, we call the series of chiral charges the multi-gap chiral charge $\mathbf{C} = (C_1, C_2, \dots, C_{N-1})$, which includes one integer for each band gap; see Fig. 1(c). From here, the bulk-boundary correspondence specifies that in gap i there are C_i chiral surface states, so called Fermi arcs. These states are called chiral because of the presence of a net nonzero number of left/right moving quasi-particles for a chosen chemical potential along a closed path in the surface Brillouin zone. In the multi-gap case, there are a net nonzero number right/left movers in multiple gaps, leading to chiral Fermi arcs that are stacked in the energy direction; see Fig. 1(d). In light of the duality of the bulk-boundary correspondence, a Fermi arc ladder is both a topologically protected emergent structure and a characteristic signature of higher-fold topology. Therefore, the Fermi arc ladder constitutes a key property of higher-fold chiral fermion materials.

In the search for an ideal material candidate to study multi-gap topology, we consider crystals in structurally chiral space group $P2_13$ (#198), where non-zero Chern numbers and bulk cone-like dispersions have recently been observed [23–28]. Materials in this space group are especially promising because the conical bands are predicted to arise from a three-fold chiral fermion at the Γ point and a four-fold chiral fermion at the R point of the bulk Brillouin zone, naturally providing a platform for multiple topological band gaps [15, 16]; see 1(e)-(g). However, no previous work has measured chiral modes in multiple band gaps, leaving the multi-gap chiral charge an open question.

In the present study, we have chemically engineered the substitutional alloy $\text{Rh}_x\text{Ni}_y\text{Si}$; see Sec. A of the Supplemental Materials. Rigorous Laue, as well as single crystal, x-ray diffraction measurements show that our sample is crystalline, and possesses the desired structurally chiral space group $P2_13$ (#198); see Sec. B of Supplemental Material. Detailed chemical analysis indicates that the composition of our sample is $x = 0.95$ and $y = 0.05$. The Flack factor was refined to $-0.01(11)$ throughout the sample, indicating that only one structurally chiral domain is

present. Importantly, the presence of Ni does not induce any magnetism as the sample was found to be diamagnetic down to 10 K.

Having verified the high quality of our samples, we now present experimental ARPES evidence of nontrivial multi-gap topology in $\text{Rh}_x\text{Ni}_y\text{Si}$. By utilizing 85 eV incident photons, the measured (001) Fermi surface covers multiple surface Brillouin zones; see Fig. 2(a). Long states are observed stretching across each Brillouin zone from the $\bar{\Gamma}$ point to the \bar{M} point. Further decreasing the photon energy to 40 eV to improve energy and momentum resolution, we find these states disperse in the same manner; see Fig. 2(b). Further understanding of these states can be gained by analyzing their E_B vs k dispersion through and on either side of the $\bar{\Gamma}$ point. At negative k_y , one isolated right-moving chiral mode is observed, which corresponds to a Chern number of $C(k_y < 0) = +1$ along this direction; see Fig. 2(c). At $k_y = 0$, the chiral state and its time-reversal partner connect directly to the projection of the degeneracy point, see Fig. 2(d). Moving to positive k_y , one isolated left-moving chiral mode is observed, indicating $C(k_y > 0) = -1$; see Fig. 2(e). Together, these three dispersions provide strong evidence that the surface states are topological Fermi arcs, connecting bands 2 and 3 of the bulk three-fold chiral fermion. Moreover, these measurements reveal the detailed nature of Fermi arc switching at a higher-fold fermion. For the first time, we clearly see a surface state transition from topological (connecting bands 2 and 3) to trivial (starting and ending at band 2) as the E_B vs k dispersion is scanned across the degeneracy point, as illustrated in the schematics in Figs. 2(f)-(h). To extract the chiral charge for gap 2, we note that the difference between the Chern numbers along two lines is equal to the chiral charge enclosed by those lines [29]. In this case, we obtain that the chiral charge is $C_2 = C(k_y < 0) - C(k_y > 0) = 1 - (-1) = 2$.

To explain how the Chern number switches back to +1 when k_y is further increased across the Brillouin zone boundary, we note that another higher-fold chiral fermions exists at the R point, not explored in this work [15, 16, 23–26].

To search for a second Fermi arc, we examine the band structure below the Fermi level and closer to $\bar{\Gamma}$. A constant E_B contour measured at $E_B = 300$ meV shows signatures of multiple chiral modes indicated by the dashed cyan lines; see Fig. 3(a). While the Fermi arcs in gap 2 are still present near the edge of Fig. 3(a), there is another set of states residing closer to $\bar{\Gamma}$. To better resolve these states, we take the second derivative of the constant E_B spectrum in Fig. 3(b), and observe that the inner states are disconnected and distinct from the outer Fermi arcs. This is consistent with these states being two sets topological Fermi arcs. Comparing to the *ab initio*

calculation, we find the top the inner states, closest to $\bar{\Gamma}$, exist in Gap 1, whereas the outer states are in Gap 2, as expected; see Fig. 3(c),(d). To confirm the topological nature of these states, we measure E_B vs k ARPES spectra along the path indicated by the dashed, dark blue line in Fig. 3(a). We identify two distinct chiral modes; see Fig. 3(e). The separation of the lower state is clear when observing the second derivative of of the data; see Fig. 3(f). By comparing to the *ab initio* calculation we confirm that the lower chiral mode disperses in Gap 1 and connects the lower bulk band to the upper bulk band, and that the upper chiral mode disperses through Gap 2; see Fig. 3(g),(h). The upper state is the Fermi arc previously explored in Fig. 2. The lower chiral state is a second Fermi arc. With an identical procedure to that carried out for Gap 2, the contribution to the multi-gap chiral charge for Gap 1 can be experimentally assigned to be $C_1 = 2$.

Our data reveals a stacked pattern of chiral modes in different bulk bandgaps, which constitutes a direct observation of a two-rung Fermi arc ladder. These Fermi arcs are expected to connect directly to the bulk states of the higher-fold chiral fermion. Already, such bulk-to-arc connections have been shown to give rise to novel transport response in one-gap topological crystals [30]. In multi-gap topological crystals, the possible electron orbits become more complex, which may be accompanied by more exotic transport properties, since multiple nontrivial topological inter-band gaps may be present at the Fermi level if the bulk bands possess adequate bandwidth. Additionally, a Fermi arc ladder naturally lends itself to optical studies investigating inter-gap topological surface state transitions.

In conclusion, by utilizing surface sensitive ARPES measurements, we have directly observed a novel Fermi arc ladder and determined the multi-gap chiral charge of a higher-fold chiral fermion: $\mathbf{C} = (2, 2)$. These results are a remarkable example of the role of topology in naturally emergent structure. By extending topological phases from one-gap to multi-gap systems, our work motivates further transport and optical research on topological intergap phenomena, which may lead to breakthroughs in surface science and quantum sensing. Furthermore, the higher-fold/multi-gap topology presented here is not restricted to electronic crystals, and can be realized in mechanical, phononic, and photonic systems, opening up opportunities for further research.

[1] Haldane, F. D. M. Nobel lecture: Topological quantum matter. *Rev. Mod. Phys.* **89**, 040502 (2017).

[2] Hasan, M. Z. & Kane, C. L. Colloquium: Topological insulators. *Rev. Mod. Phys.* **82**, 3045 (2010).

- [3] Qi, X.-L. & Zhang, S.-C. Topological insulators and superconductors. *Rev. Mod. Phys.* **83**, 1057 (2011).
- [4] Ando, Y. & Fu, L. Topological crystalline insulators and topological superconductors: From concepts to materials. *Annu. Rev. Condens.* **6**, 361-381 (2015).
- [5] He, K., Wang, Y., Xue, Q.-K. Topological materials: Quantum anomalous hall system. *Annu. Rev. Condens.* **9**, 329-344 (2018).
- [6] Tokura, Y., Yasuda, K. & Tsukazaki, A. Magnetic topological insulators. *Nat. Rev. Phys.* **1**, 126-143 (2019).
- [7] Armitage, N. P., Mele, E. J., & Vishwanath, A. Weyl and Dirac semimetals in three-dimensional solids. *Rev. Mod. Phys.* **90**, 015001 (2018).
- [8] Hasan, M. Z., Xu, S.-Y., Belopolski, I. & Huang, S.-M. Discovery of Weyl fermion semimetals and topological Fermi arc states. *Annu. Rev. Condens.* **8**, 289-309 (2017).
- [9] Yan, B., & Felser, C. Topological materials: Weyl semimetals. *Annu. Rev. Condens.* **8**, 337-354 (2017).
- [10] Burkov, A. A. Weyl metals. *Annu. Rev. Condens.* **9**, 359-378 (2018).
- [11] Mañes, J. L. Existence of bulk chiral fermions and crystal symmetry. *Phys. Rev. B* **85**, 155118 (2012).
- [12] Wieder, B. J., Kim, Y., Rappe, A. M. & Kane, C. L. Double Dirac semimetals in three dimensions. *Phys. Rev. Lett.* **116**, 186402 (2016).
- [13] Bradlyn, B. *et al.* Beyond Dirac and Weyl fermions: Unconventional quasiparticles in conventional crystals. *Science* **353**, aaf5037 (2016).
- [14] Chang, G. *et al.* Topological quantum properties of chiral crystals. *Nat. Mater.* **17**, 978-985 (2018).
- [15] Chang, G. *et al.* Unconventional chiral fermions and large topological Fermi arcs in RhSi. *Phys. Rev. Lett.* **119**, 206401 (2017).
- [16] Tang, P. *et al.* Multiple types of topological fermions in transition metal silicides. *Phys. Rev. Lett.* **119**, 206402 (2017).
- [17] de Juan, F. *et al.* Quantized circular photogalvanic effect in Weyl semimetals. *Nat. Commun.* **8**, 15995 (2017).
- [18] Nandy, S., Sengupta, K. & Sen, D. Transport across junction of pseudospin-one fermions. *Phys. Rev. B* **100**, 085134 (2019).
- [19] Chang, G. *et al.* Nexus fermions in topological symmorphic crystalline metals. *Sci. Rep.* **7**, 1688 (2017).
- [20] Weng, H. *et al.* Topological semimetals with triply degenerate nodal points in Θ -phase tantalum ni-

- tride. *Phys. Rev. B* **93**, 241202(R) (2016).
- [21] Zhu, Z. *et al.* Triple point topological metals. *Phys. Rev. X* **6**, 031003 (2016).
- [22] Lv, B. Q. *et al.* Observation of three-component fermions in the topological semimetal molybdenum phosphide. *Nature* **546**, 627-631 (2017).
- [23] Sanchez, D. S. *et al.* Topological chiral crystals with helicoid-arc quantum states. *Nature* **567**, 500-505 (2019).
- [24] Rao, Z. *et al.* Observation of unconventional chiral fermions with long Fermi arcs in CoSi. *Nature* **567**, 496-499 (2019).
- [25] Schröter, N. B. M. *et al.* Chiral topological semimetal with multifold band crossings and long Fermi arcs. *Nat. Phys.* **15**, 759-765 (2019).
- [26] Takane, D. *et al.* Observations of chiral fermions with large topological charge and associated Fermi-arc surface states in CoSi. *Phys. Rev. Lett.* **122**, 076402 (2019).
- [27] Xu, X. *et al.* Crystal growth and quantum oscillations in topological chiral semimetal CoSi. *Phys. Rev. B* **100**, 045104 (2019).
- [28] Rees, D. *et al.* Observation of topological photocurrents in the chiral Weyl semimetal RhSi. Preprint at <https://arxiv.org/abs/1902.03230> (2019).
- [29] Belopolski, I. *et al.* Criteria for directly detecting topological Fermi arcs in Weyl semimetals. *Phys. Rev. Lett.* **116**, 066802 (2016).
- [30] Moll, P. J. W. *et al.* Transport evidence for Fermi-arc-mediated chirality transfer in Dirac semimetal Cd₃As₂. *Nature* **535**, 266-270 (2016).

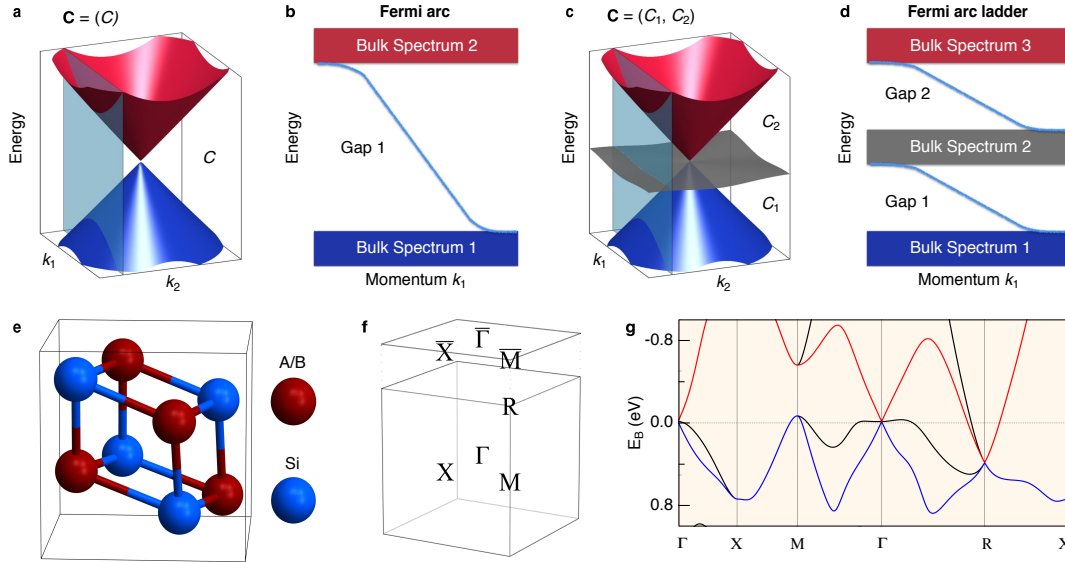


FIG. 1: **Multiple nontrivial band gaps and Fermi arc ladders in $P2_13$ materials.** **a**, Schematic of a two-band system, with degeneracy corresponding to a Weyl fermion in three dimensions. **b**, Schematic of bulk-boundary correspondence of a one-gap system with a surface/edge chiral mode. The momentum path corresponds to the blue plane in **a**. **c**, Schematic of a chiral fermion with three bulk cones and two topologically nontrivial energy gaps. **d**, Schematic of bulk-boundary correspondence of a two-gap system with surface/edge chiral modes. The momentum path can be visualized as the blue plane in **c**. **e**, Crystal structure of A_xB_ySi substitution alloy in the $P2_13$ spacegroup (#198). **f**, Bulk and (001) surface Brillouin zone. **g**, *Ab initio* band structure calculation along high-symmetry lines of RhSi binary.

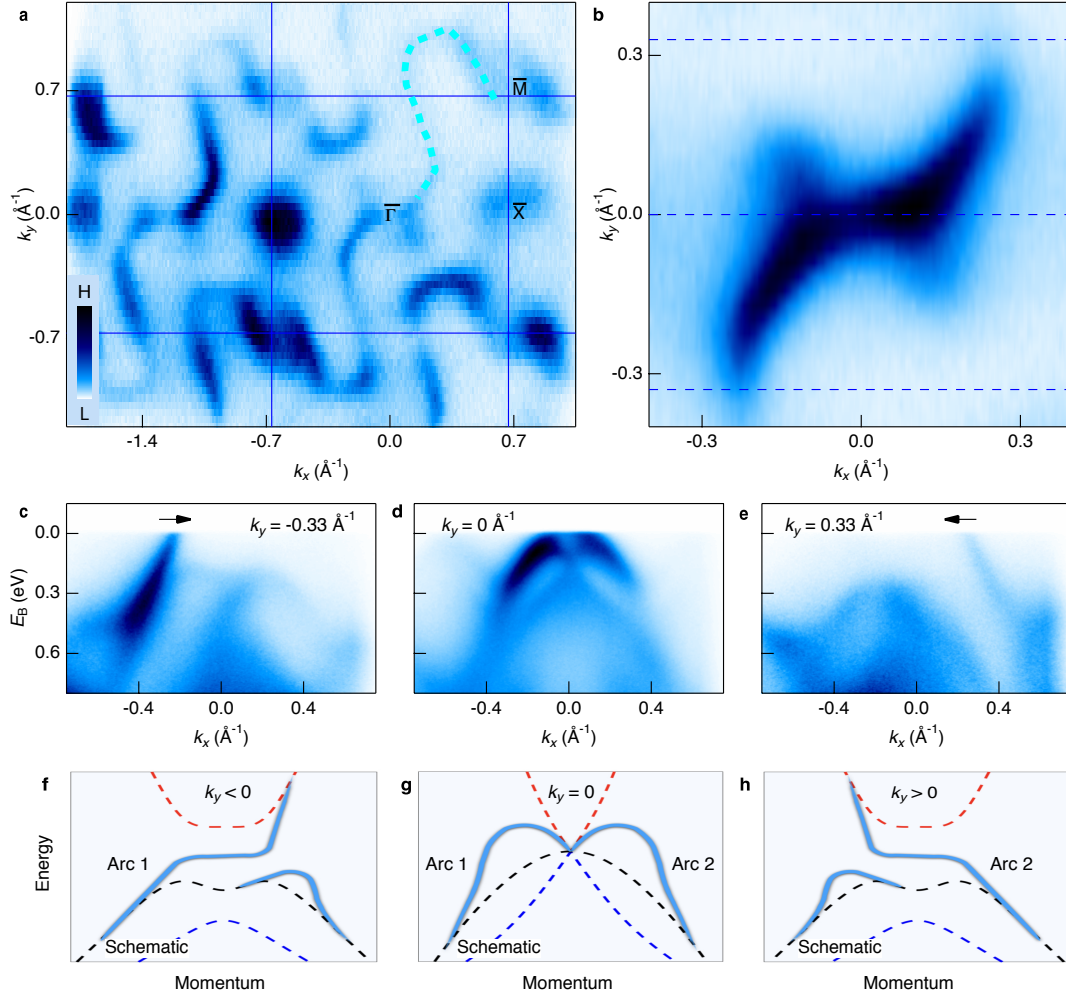


FIG. 2: Fermi arc switching in momentum space. **a**, Surface sensitive ARPES measured Fermi surface from (001) surface, measured with 85 eV incident photons. Long Fermi arc surface states connect pockets at $\bar{\Gamma}$ and \bar{M} as indicated by the dashed cyan line. **b**, ARPES measured Fermi surface at the $\bar{\Gamma}$ point with 40 eV incident photons. **c-e**, E_B vs k ARPES spectra showing chiral Fermi arc surface states along paths defined by the dotted lines in **b**. Arrows indicate chiral modes at the Fermi level, which switch at the three-fold chiral fermion at $\bar{\Gamma}$. **f-h**, Schematics of chiral Fermi arcs (solid blue lines) and bulk bands (dotted lines) depicting the Fermi arc switching at the $\bar{\Gamma}$ point in gap 2.

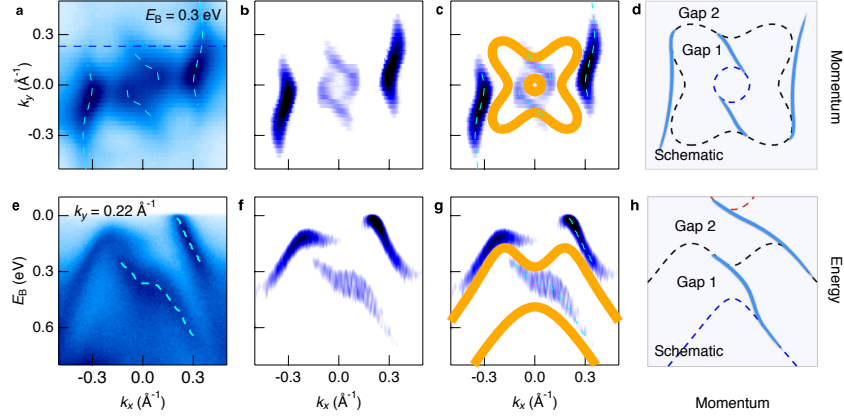


FIG. 3: **A two-rung Fermi arc ladder.** **a, b**, ARPES measured constant E_B contour at $E_B = 300$ meV (**a**) and second-derivative (**b**) at the $\bar{\Gamma}$ point. Two states near the zone center are observed, disconnected from the outer Fermi arcs. Both inner and outer states are indicated by cyan dashed lines in **a**. **c**, Same data as in **b** with an overlay of the *ab initio* band structure at $k_z = 0$. **d**, Schematic constant E_B contour showing chiral states (thick blue lines) in gap 1 and gap 2 of the bulk bands of the three-fold chiral fermion (dotted lines). **e, f**, ARPES measured E_B vs k cut at $k_y = 0.22 \text{ \AA}^{-1}$ (**d**) and second-derivative (**e**), along the path indicated by the dark blue dashed line in **a**. Two disconnected chiral modes are observed as indicated by the dashed cyan lines. **g**, Same data as in **f** with an overlay of the *ab initio* band structure at $k_z = 0$. **h**, Schematic E_B vs k plot showing the Fermi arc ladder (thick blue lines) with states propagating in gap 1 and gap 2 of the three-fold chiral fermion (dotted lines). The trivial surface state has been suppressed for clarity.

Acknowledgements

Work at Princeton University and Princeton-led synchrotron based ARPES measurements were supported by the Gordon and Betty Moore Foundation through the EPIQS program Grant No. GBMF4547-HASAN and by the National Science Foundation under Grant No. NSF-DMR-1507585. This research used resources of the Advanced Light Source, which is a DOE Office of Science User Facility under contract No. DE-AC02-05CH11231. T.A.C. was supported by the National Science Foundation Graduate Research Fellowship Program under Grant No. DGE-1656466. K. M. and C. F. thank the financial support of the European Research Council (ERC) with Advanced Grant No. (742068) TOP-MAT.

Supplementary Materials

SM A. Methods

Single Crystal Growth

A single crystal of the $\text{Rh}_x\text{Ni}_y\text{Si}$ was grown from the melt using the vertical Bridgman crystal growth technique. First, polycrystalline ingot of the Ni-substituted composition, $\text{Rh}_{0.95}\text{Ni}_{0.05}\text{Si}$ was prepared by pre-melting the highly pure stoichiometric amount of respective metals under argon atmosphere using an arc melt technique. Then the crushed powder was filled in a custom-designed sharp-edged alumina tube, which was again sealed inside a tantalum tube with argon atmosphere. Here we induced a slight excess of Si in the composition to ensure a flux growth inside the Bridgman ampule. First, the sample was heated to 1550°C with a rate of 200 C/h and held there for 10 h. Then the ampule was slowly pulled to the cold zone, up to 1100°C with a rate of 0.8 mm/h . The temperature was controlled by attaching a thermocouple at the bottom of the Bridgman ampule. A single crystal with average dimension of 9 mm length and 6 mm diameter was obtained.

Angle-resolved photoemission spectroscopy

(001) polished single crystals were *in situ* sputtered with 500-1000 eV Ar ions for 5-30 minutes and annealed to $550\text{-}585^\circ\text{C}$ (assuming a sample emissivity of 0.45) for 30-45 minutes in ultra-high vacuum (UHV), cyclically.

ARPES studies were carried out at beamline 4.0.3 of the Advanced Light Source. Incident light in the range 40-85 eV. Sample temperature was maintained between 17-20 K during all ARPES measurements and vacuum conditions were UHV.

SM B. Single-crystal characterization

The single crystallinity was first checked with a white beam backscattering Laue x-ray setup at

room temperature. A picture of the grown single crystal and the refined Laue pattern is shown in Fig. S1(a),(b). In order to verify the presence of Ni, Rh, and Si in the grown single crystal, we first performed the compositional analysis with energy-dispersive X-ray (EDX) spectroscopy and a representative plot is shown in Fig. S1(b), clearly revealing the presence of all three elements in the compound. Then a detailed chemical analysis was carried out to precisely determine the chemical composition of the grown single crystal and is estimated as $\text{Rh}_{0.955}\text{Ni}_{0.045}\text{Si}$.

A small piece was broken from the large crystal and selected fragments were mounted on Kapton loops and tested for structure refinement. Data were collected on a Rigaku AFC7 four-circle diffractometer with a Saturn 724+ CCD-detector applying graphite-monochromatized $\text{Mo-K}\alpha$ radiation. The pertinent details are given in Table S1. Due to strong correlations, a free refinement of occupancies at the mixed Rh/Ni site did not give very reasonable results as indicated in particular by comparison of displacement parameters at Si versus Rh/Ni atom site. Since in binary RhSi counterintuitively the displacement parameter of Si is slightly smaller than at the other site, occupancies for the metals were optimized using this condition as a main guide. Along this line, an optimized model indicates 7% Ni at the metal site which is in quite good agreement with analytical results, even more when considering large difference in scattering power of Ni vs. Rh. The absolute structure of the crystal clearly has to be assigned to B-form [31] and the Flack parameter refined to -0.01(11). Evidently, the refined Flack parameter confirms single chirality domain formation in the grown single crystal. As expected the absolute structure refinement is not particularly sensitive to variation of occupancies at the metal site.

The magnetization measurement was performed using a Quantum Design vibrating sample magnetometer (MPMS) with magnetic field up to 7 T. The diamagnetic behavior of the $\text{Rh}_x\text{Ni}_y\text{Si}$ single crystal is evident from the field dependent magnetization data at various temperatures 5, 20 and 50 K; see Fig. S1(c). Similar diamagnetic behavior is also observed for the Weyl fermions in TaAs [32] and the Dirac fermions in Bi [33, 34]. The field-independent negative dc-susceptibility throughout the measured temperature range indicates the absence of any long range magnetic ordering and confirms the intrinsic diamagnetism in our $\text{Rh}_x\text{Ni}_y\text{Si}$ single crystals; see Fig. S1(d).

SM C. Ab initio calculation

First-principles calculations were performed within the density functional theory (DFT) framework using the projector augmented wave method as implemented in the VASP package [35, 36].

A Γ -centered k-point $17 \times 17 \times 17$ mesh was used.

- [31] Spence, H. C. H. *et al.* On the minimum number of beams needed to distinguish enantiomorph in X-ray and electron diffraction. *Acta Cryst.* **A50**, 647-650 (1994).
- [32] Liu, Y. *et al.* Intrinsic diamagnetism in Weyl semimetal TaAs. *J. magn. Magn. Mater.* **408**, 73-76 (2016).
- [33] Shoenberg, D. & Uddin, M. Z. The magnetic properties of bismuth. II-The de Haas-van Alphen effect. *Proc. R. Soc. London Ser. A* **156**, 701-720 (1936).
- [34] Fuseya, Y., Ogata, H. & Fukuyana, H. Transport properties and diamagnetism of dirac electrons in bismuth. *J. Phys. Soc. Jpn.* **84**, 012001 (2015).
- [35] Kresse, G. & Furthmüller, J. Efficient iterative schemes for *ab initio* total-energy calculations using a plane-wave basis set. *Phys. Rev. B* **54**, 11169 (1996).
- [36] Kresse, G. & Joubert, D. From ultrasoft pseudopotentials to the projector augmented-wave method. *Phys. Rev. B* **59**, 1758 (1999).

Compound	Rh _x Ni _y Si
F.W. (g/mol);	127.91
Space group;Z	P2 ₁ 3 (No.198);4
<i>a</i> (Å)	4.6766(6)
<i>V</i> (Å ³)	102.28(4)
Absorption Correction	Multi-scan
Extinction Coefficient	0.22(1)
<i>θ</i> range (deg)	4.4-36.8
No. independent reflections	165
No. parameters	8
<i>R</i> ₁ ; <i>wR</i> ₂ (all)	0.0212; 0.0464
Goodness of fit	1.122
Diffraction peak and hole (e ⁻ /Å ³)	1.188;-1.476
Refined formula	Rh _{0.93} Ni _{0.07} Si

Table S1: **Single crystalline x-ray diffraction.**

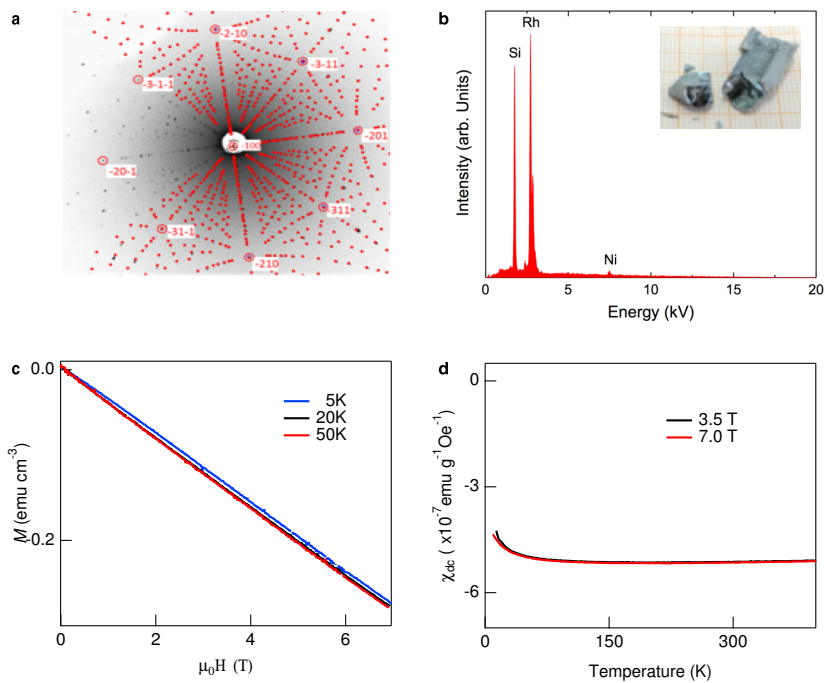


FIG. S1: Physical characterization of $\text{Rh}_x\text{Ni}_y\text{Si}$ single crystals. **a**, Laue diffraction pattern of a $[100]$ oriented crystal superposed with a theoretically simulated pattern confirming high crystal quality. **b**, EDX pattern of the $\text{Rh}_x\text{Ni}_y\text{Si}$ single crystals. Picture of the grown $\text{Rh}_x\text{Ni}_y\text{Si}$ single crystal (inset). **c**, Magnetization measured at 5, 20, and 50 K. **d**, Magnetic susceptibility measured with 3.5 and 7 T fields, respectively.